A Thermal, Hydrological and Mechanical Model of Patua Geothermal Field, Nevada

Torquil Smith[1], Eric Sonnenthal[1], Nori Nakata[1], Trenton Cladouhos[2], Michael Swyer[3]

[1]Lawrence Berkeley National Laboratory, Berkeley, California

[2]Formerly; Cyrq Energy, Salt Lake City, Utah

[3]Cyrq Energy, Salt Lake City, Utah

JTSmith@lbl.gov

Keywords: Hydrological Simulation, Patua geothermal field, native-state model

ABSTRACT

A Thermal-Hydrological-Mechanical (THM) model is being developed for the Patua geothermal field in Nevada. The purpose of the model is to help integrate observed surface deformation (LIDAR, GPS), MEQs, subsurface stress, and regional strain rate data to evaluate deformation of the field for potential stimulation. A new permeability model was constructed to approximate native-state temperatures, first by reevaluating existing geologic and fault data, and then by calibrating TH properties. A set of 71 fault picks from well logs (Pollack, 2021) combined with a set of drilling lost circulation zone (LCZ) observations (Cladouhos et al., 2017) produced 76 prospective fault-well intersection points. This was analyzed using a gridded search for the orientation of planes with the maximum number of fault picks and LCZ depths in a plane (within a 25 m tolerance). After fitting five of the six points closest to Patua Hot Springs with a plane (within 25 m tolerance), a plane striking N 108.8 E dipping 68.9 was used to divide the remaining picked points into a northeastern set and the remainder for separate analysis. In subsequent stages, at each stage the plane with maximum weighted number of picks in a 50 m thick zone was selected, and the remaining data on either side was analyzed separately. In the maximizations, the number of points fit was weighted by $1/[\tan(dip) + 4.2/\tan(dip)] + 1/4.2npts$ to lessen sampling bias due to roughly common well orientation (near vertical) and to limited well depth compared to lateral sampling extent. This yielded a set of 12 planes fitting 3 to 10 points each, fitting 69 of the 76 points total. The faults were assumed to be centered on the mean of the fitted intersection points in strike and dip directions, and fault strike length and dip breadth was taken as sqrt(12) times the square root of the intersection point variances in strike and dip directions respectively, somewhat arbitrarily for faults sampled by well intersection, but rigorous for rectangular fault patches sampled randomly (uniformly).

Initially, unfaulted reservoir rock was given 10^{-15} m^2 (E-W, vert) and 10^{-16} m^2 (N-S) permeabilities, with 10^{-15} m^2 horizontal permeability at elevations above 100 m depth in the central part of the study area (i.e., above 1150 m elev.), with fault permeabilities from 20 x 10^{-15} to 125 x10^{-15} m^2, in a simple 5 fault model based on an extension (M. Swyer, 2017, Cyrq Energy internal document) of the Cladouhos et al. (2017) conceptual model. Faults were modelled as connected sequences of regular grid blocks (100 x 100 x 100 m at grid center). Initial permeabilities were selected based on the Garg et al. (2017) and Murphy et al. (2017) reservoir models for Patua. A 251.5°C temperature at -3550 m elevation (~4800 m depth) was assumed based on extrapolation of one of the deeper wells. Following earlier studies, an inhomogenous zone of increased temperature was presumed at the base, here with 10°C amplitude maximum increase above background, smoothly decreasing to no increase 3 km laterally from the inhomogeneity center. Permeabilities were modified to a 2 x 10^{-15} to 10^{-14} m^2 range for the faults and 1.2 x10^{-16} to 1.9 x10^{-16} (E-W, vert.), 3.8x10^{-16} (N-S) background, with 10^{-15} m^2 horizontal permeability above 1150 m elevation, through many intermediate values, in an attempt to fit interpolated native-state (e.g., soon after drilling) well temperature profiles at -1200 m elevation (~2450 m depth at the center of the study area), and +1150 m elevation, as well as the general trends of the set of well temperature profiles. Indifferent agreement led to reconsidering the underlying fault model, re-analysis of the fault pick and LCZ data, and subsequent adoption of the 12 fault plane model above, initially with the same background permeabilities as attained in the simpler 5 fault model, and fault permeabilities of 0.5-2 x 10^{-15} m^2.

Calibrated fault permeabilities range from 2-60 x 10^{-15} m^2, with surficial layers having a horizontal permeability reduced to 7.5 x 10^{-16} m^2. To facilitate convective upwelling with a smaller artificial bottom boundary temperature perturbation (10°C maximum increase over background), seven of the modelled faults were extended downwards to -2925 m elevation: those not intersecting others on extension. Simulation temperatures at reservoir depth (1005 m below sea level) match observations within about 10°C, at shallow depth (1107 m elev.) to about 20°C.

1. INTRODUCTION

A Thermal-Hydrological-Mechanical (THM) model is being developed for the Patua geothermal field in Nevada. The purpose of the model is to help integrate observed surface deformation (LIDAR, GPS), MEQs, subsurface stress, and regional strain rate data to evaluate deformation of the field for potential stimulation. A number of authors have modelled hydrological flow at the Patua geothermal field (e.g., Garg et al., 2015; Murphy et al., 2017), based on native-state temperature data, some flow test data and in the latter case, some tracer test data also. Cladouhos et al. (2017) provide a three fault segment conceptual model for flow along faults at Patua, based on zones of fluid loss during drilling (lost circulation zones, LCZ) and tracer data. Pollack (2020) and Pollack et al. (2021) extended the set of 33 LCZ points of Cladouhos et al. (2017), adding additional points at large fractures intersected by wells at Patua (71 `fault markers'), and made a broad suite of somewhat larger scale structural models based on these and gravity and magnetic data. Here,

fault locations are re-estimated using the extended set and used to construct a permeability model. A novel porosity estimation method is introduced for estimating porosity in the layers overlaying the fractured granitic basement thermal reservoir. Average well log velocities and densities are used to estimate bulk and shear moduli, and scaled using moduli measured for granite core from fairly nearby locations. Fault and background permeabilities were adjusted to give native-state temperatures in simulations. The study area has broad valley floors at about 1250 m elevation, and topography rising to 1500 m. For modelling, topography was truncated at 1450 m.

2. ESTIMATION OF FAULT/FRACTURE MODEL

We use a combined set of the Pollack et al. (2021) fault markers and the Cladouhos et al. (2017) LCZ points (76 intersection points total) to estimate a set of 12 fault or fracture planes intersecting the wells at Patua. The first of these was found fitting a plane (striking N 18.2 E UTM) to the 6 closest points to Patua Hot Springs, and removing the points from further consideration. Subsequently, in principal, a sequence of planes was found, at each stage making a gridded search of prospective plane orientations to find the plane with the greatest (weighted) number of intersection points within a 25 m tolerance of the plane, splitting the remaining points (outside tolerance) into those above, and those below the plane, and repeating on each sub-group. The number of intersection points within tolerance was weighted to counteract sampling bias due to a preponderance of near vertical wells and, due to a greater horizontal than vertical extent of the volume sampled by wells, using an ad hoc value

$$\frac{1}{tan\theta+\frac{4.2}{tan\theta}}+\frac{1}{4.2\,n_p}, \tag{1}$$

where θ is prospective fault dip angle, and n_p is the number of points in the (sub-)group under consideration. A simpler version, without weighting and without successive splitting of remainder points into two groups, was used by Smith et al. (2021) to estimate fault planes from enhanced geothermal stimulation (EGS) micro-earthquakes and aftershock sequences.

In practice, to get a set of plane segments closer in distribution to an unpublished five fault extension of the Cladouhos et al. (2017) conceptual model, the intersection points were artificially separated into two groups, and the procedure was performed separately on each. The points were separated into those on or below a plane striking N 108.8 E, dipping 68.8 degrees, (i.e., NE of the plane) and those above it. Of those on or below, those more than 300 m along strike from the average were placed together with those above that plane. The separating plane itself was from application of the method on the unseparated points. Plane segment edges along strike and up- and down-dip were set from the average of points within tolerance of a plane and $\pm$ (variance/12)$^{1/2}$ of them along strike and along dip. The plane edge estimates are rigorous for plane segments sampled by uniformly distributed random points, and would be rigorous for randomly located wells (under a uniform distribution). Down-dip edge and up-dip edge locations were subsequently adjusted, assuming that faults not intersecting others below themselves extend to -2927 m elevation, and faults striking -137.1 and -158.8 deg. extended +-200 m along strike to encompass two intersection points missed otherwise. The 12 planes found fit 69 of the 76 intersection points within tolerance, with 3 to 10 points each. Plane coordinates relative to UTM zone 11, NAD 83 coordinates, shifted by (-320000, -4380000) m in Easting and Northing, are given in Tables 2 and 3 in the Appendix. At Patua, UTM Northing is approximately 1.3 degrees west of true North. The remaining 7 intersection points are in various of the sub-groups of left over from finding the above 12 faults, and we consider them insufficient to estimate further fracture planes. The plane striking N 127.1 E (UTM) is supported by only 3 intersection points, so is somewhat speculative. The faults are shown in plan view in Figure 1. Grid blocks with faults passing through them were treated as fault material.
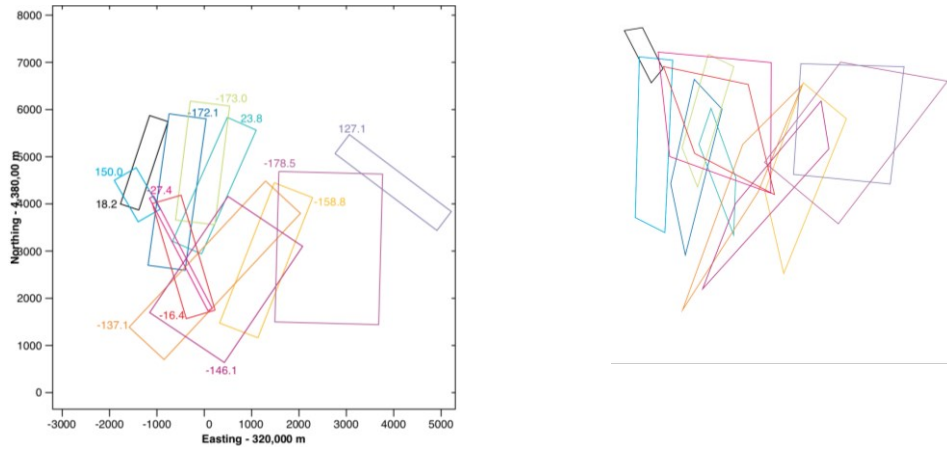

Figure 1: Left: Plan view of estimated faults, labeled by fault strike (deg.). Faults dip to right when viewed in strike direction. Right: Perspective view looking slightly downwards from SE, from (-2500, -3000, 1500) m.

3. ESTIMATION OF OVERBURDEN AND RESERVOIR POROSITY

Compression (P) wave and shear (S) wave slowness (1/velocity) logs and density logs were available for two wells [85-19 and 58-29, with wellheads at (3801,1251) and (622,1423) m respectively], and 25 m vertical interval averages were made. The eigenvalues and eigenvectors of the cross power matrix of sum $(S_p', S_s')^t (S_p', S_s')$, where (S_p', S_s') is a pair of normalized P wave and S wave slownesses, with S_p' and S_s' de-meaned and normalized by their respective root mean squared averages, imply that the linear combination $S_{pr} == S_p + 0.4282\,S_s$ encompasses 96% of the power in S_p' and S_s', so it is a useful combination. 25 m averages of S_{pr} are plotted as a function of

bulk density in Figure 2. There is a tendency for sets of points to plot on lines with a slope of approximately 0.653 x10^{-6} s/m / (kg/m^3). Surmising that these are sets of rocks of constant composition and varying porosity, a model of grain density was developed and calibrated against samples of known density, porosity and composition from nearby Desert Peak geothermal site [Lutz et al. (2010), as in Sonnenthal et al. (2018)], giving

$$\rho_{gr} = \rho_{ref} + \beta \,, \tag{2}$$

$$\beta = \left(S_{pr} - S_{ref} + \eta_c \rho_{ref} - \eta_c \rho \right) / (\eta_{poro} - \eta_c) \,, \tag{3}$$

where η_c = -0.6495 x10^{-6} m^2 s/kg is $\partial\, S_{pr}\, /\, \partial\, \rho_{bk}$ along lines of assumed constant composition, η_{poro} = 0.1305 x10^{-6} m^2 s/kg is $\partial\, S_{pr}\, /\, \partial\, \rho_{bk}$ at zero porosity from S_{pr} extrapolated assuming constant composition, ρ_{ref} = 2424. kg/m^3 (Desert Peak tuff grain density), S_{ref} = 0.261x10^{-3} s/m (Desert Peak tuff S_{pr}, adjusted for using with dynamic moduli in place of static moduli) and ρ_{bk} is bulk density. This yields an estimate of porosity ϕ from S_p and S_s, bulk density and Eqs. (2-3);

$$\phi = \left(\rho_{bk} - \rho_{gr} \right) / \left(\rho_{wat} - \rho_{gr} \right) \,, \tag{4}$$
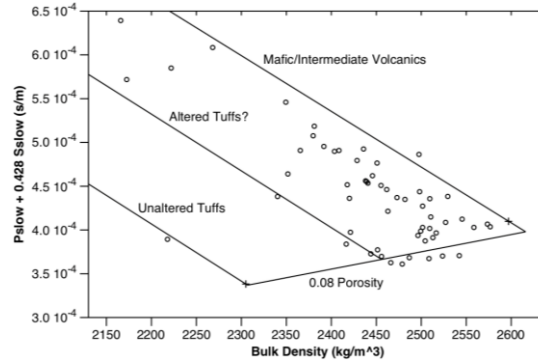
where ρ_{wat} is water density.

Figure 2: 25 m averaged P and S wave slowness combination S$_p$ + 0.4282 S$_s$ as a function of averaged bulk density, for rocks above the granitic basement (reservoir). Identification of lines 'mafic/intermediate volcanics' and 'unaltered tuffs' based on calibration samples from Desert Peak at two crosses.

Below 500 m below sea level (-500 m elevation, ~1750 m depth) material is treated as the fractured granite of the reservoir, and porosity is estimated using the Raymer-Hunt model of P velocity/slowness to estimate porosities,

$$V_p = \phi\, V_{p\, fl} + (1 - \phi)^2\, V_{p\, gr}, \tag{5}$$

(e.g., Glover, undated, Raymer et al., 1980), where V_p is P velocity, $V_{p\, fl}$ is fluid P velocity, $V_{p\, gr}$ is grain P velocity. The granite grain P velocity was estimated from Eq. (5) assuming that average porosity at the depth of highest average P velocity (2700 m) is 0.001. Then, assuming constant $V_{p\, gr}$, Eq. (5) is solved for ϕ for V_p at other depths. Estimated porosity is plotted as a function of depth in Figure 3, together with a few core values. Many of the core values are significantly less than the estimates from Eqs. (2-4), presumably due to bias in selecting core from competent rock. The high estimated porosities presumably represent a large amount of pore water adsorbed in clays, in altered rock. Fault grid blocks are given 0.06 porosity, a middling value for estimated porosity below 1250 m depth. Given porosities and bulk densities from well logs, grain densities were also estimated and are plotted together with bulk densities in Figure 4.
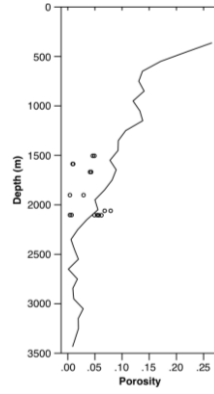
Figure 3: Estimated porosity as a function of depth; above 1750 m depth, from S_{pr}, ρ_{bk} and Eqs. (2-4), below 1750 m depth from Raymer-Hunt model V_p Eq. (6), using $V_p(2700)$ as a reference. Measured values from Patua core samples shown as circles.
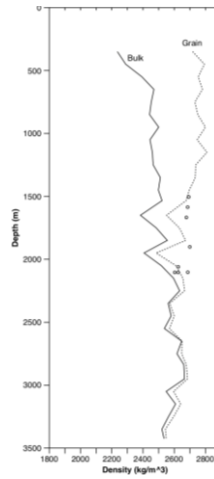

Figure 4: Solid line: 100 m average bulk density from well logs; dashed line: estimated grain density; circles: measured grain density values from core samples from Patua.

4. THERMAL CONDUCTIVITY

Also based on Figure 2, above the reservoir, an estimate of volcanics to tuffs ratio was made based on position relative to the lines marked altered tuffs and mafic/intermediate volcanics, with points at the former assumed to be 100% tuff, and at the later 100% intermediate volcanics, plotted in Figure 5. The estimate is also plotted at the depths of the reservoir granite, but is not used there Thermal conductivities k_{th} were assigned interpolating linearly between tuff conductivity and volcanics conductivity for thermal conductivity parametrized as

$$k_{th}(T) = \frac{A}{350+T} + B,$$ (6)

with A=807, B=0.64 (W/m°C) for tuffs, and A=474, B= 1.18 (W/m°C) for other volcanic, for temperature T (Celsius), following Sonnenthal et al. (2018). Temperature for thermal conductivity calculation was a quadratic fit to temperature in well 16-29 [wellhead at E, N= (-200, 1752) m], $T(z) = 112.7 - 0.06045\ z - 7.9 \times 10^{-6}\ z^2$. In the reservoir, parameters A = 738.5, B=0.64 were used, the former from fitting thermal conductivity of core from the Climax Stock granodiorite at 23°C (Izett, 1960) using the value of B from rhyolite.
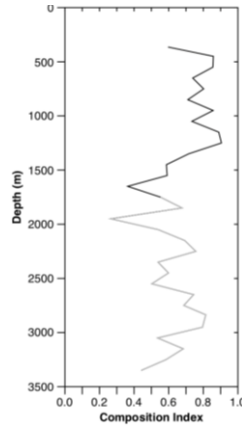
Figure 5: Solid line (above 1750 m depth): estimated relative fraction of intermediate volcanics. Dashed line (below 1750 m depth): same computed index, in zone presumed to be granite.

Specific heat was approximated as 1000 J/kg°C

5. ESTIMATION OF MECHANICAL MODULI

Bulk modulus and shear modulus were estimated from P and S wave velocity logs and density logs averaged between two wells (85-19 and 58-29), and averaged over 100 m vertical intervals. As dynamic moduli measured in well logs, and static drained moduli needed for mechanics modelling in general differ, the well log moduli averages were scaled to match moduli measured at longer period. Bulk and shear moduli were scaled by 1.08 and 0.82 respectively, so that averaged moduli at the depth of highest averaged P velocity (2700 m) match those for Climax Stock granodiorite from the Nevada Test Site (Stowe, 1969), and are plotted in Figure 6.
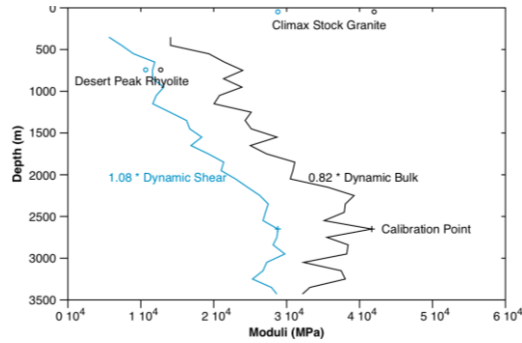

Figure 6: Scaled 100 m average bulk and shear moduli as a function of depth (averaged between wells 85-19 and 58-29). Desert Peak and Nevada Test Site (Climax stock granite) core values shown as circles.

6. BIOT COEFFICIENT

The Biot coefficient was estimated assuming a 58.5 GPa grain bulk modulus and the 100 m averaged bulk moduli of Figure (6). The grain bulk modulus was calculated for the composition of Climax Stock granodiorite given by Isherwood et al. (1982); 28.6% quartz, 45.9 % plagioclase, 16.3% orthoclase, 9.2% biotite, using tabulated moduli for quartz, feldspar and mica, from Selvadurai (2021), assuming volume weighting of 1/bulk modulus, and is plotted in Figure 7.
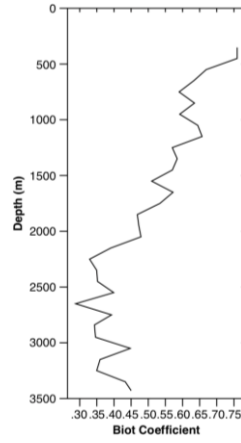
Smith et al.

Figure 7: Biot coefficient vs depth.

7. OTHER PARAMETERS

Rocks above 1150 m elevation (above ~100 m depth in flatter parts of terrain) were approximated as Quaternary sediments with permeabilities as in Table 1. These are similar to values used by Garg et al. (2015).

Table 1: Model background permeabilities, in Easting, Northing and vertical directions.

Elevation (m)	K_{xx} (m^2)	K_{yy} (m^2)	K_{zz} (m^2)	
1150 - 1450	5 x 10^{-16}	5 x 10^{-16}	0.5 x 10^{-16}	Quaternary Sediments
950 - 1150	5.6 x 10^{-16}	5.6 x 10^{-16}	1.1 x 10^{-16}	Quaternary Sediments
150 - 950	1.2 x 10^{-16}	1.2 x 10^{-16}	1.2 x 10^{-16}	Rhyolitic Tuffs
-3550 - 150	0.7 x 10^{-16}	1.5 x 10^{-16}	0.7 x 10^{-16}	(Fractured) Granite

Initial fault permeabilities were similar to values shown in Murphy et al. (2017). Fault permeabilities were adjusted to match interpolated native-state temperature values at -1005 m elevation, and more roughly at 1107 m elevation. Vertical permeabilities are shown in cross section at -1005 m elevation, and in vertical section at y (Northing) = 3050 m, in Figure 8.
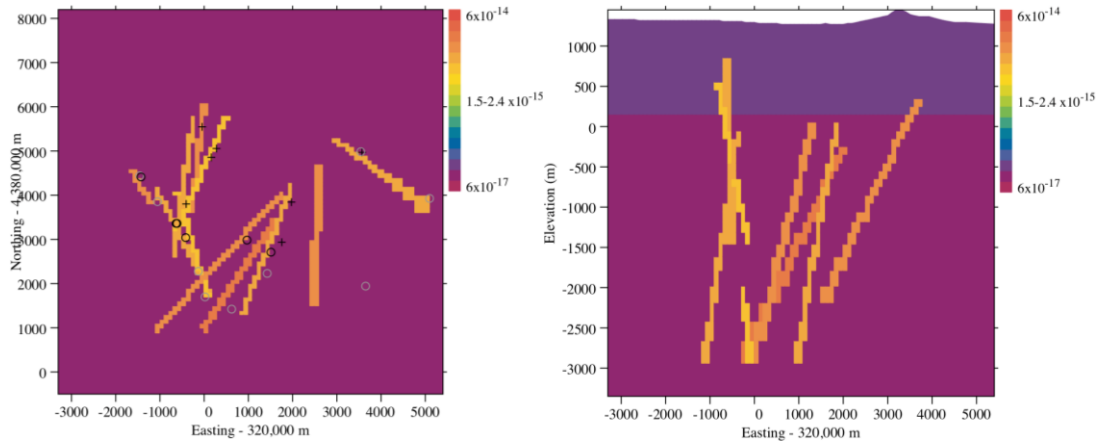

Figure 8: Left: Plan view of vertical permeability at -1005 m elevation. Injection wellhead locations: crosses; production wellhead locations: black circles; other open wellhead locations: gray circles. Right: Vertical cross section of vertical permeability at y= 3050 m, about 2x vertical exaggeration.

The modelling grid extended 12,700 m in x and y, somewhat broader than the portion plotted. Open wells were treated as being open below the top of granite surface plotted in Cladouhos et al. (2017) and extended laterally by level extension from the closest point with subsequent smoothing. Assumed top of granite ranges from -715 m elevation in the southwest to 295 m in the northeast. Wells were treated as non-existent during native-state simulations.

8. NATIVE-STATE DATA AND SIMULATION

Pre-exploitation temperatures interpolated between wells and extrapolated to 750 m from well temperature measurements are plotted in horizontal cross section at -1005 m and 1107 m elevation, in Figure 9.
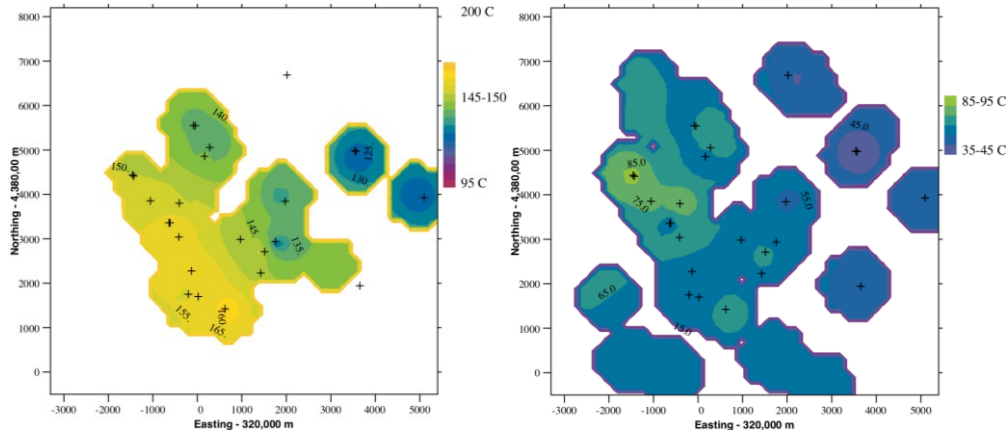

Figure 9: Left; Interpolated native-state temperatures at Patua at -1005 m elevation (reservoir depth). Right; Interpolated native-state temperatures at Patua at 1107 m elevation. Wellhead locations depicted by crosses. Temperatures are interpolated/extrapolated laterally to 750 m radius from well data locations. (Narrow plotting artifact at edges of plotted zones.)

In modelling native-state temperatures, we initialize temperatures with a -0.55°C/m vertical temperature gradient with 12.5°C temperature at 1250 m elevation (surface conditions), representing an average of nearby daily low and high temperatures. In modelling flow at Patua previous investigators have found it expedient to place either inhomogeneous heat flux, or inhomogeneous temperature boundary conditions at the bottom of the model to help induce hydrothermal circulation and elevated temperatures about the production zones at Patua. As previously mentioned, we extended near-vertical faults to -2927 m elevation to help hydrothermal circulation to achieve observed temperatures, although their depth extent is unknown. The deepest well extends to about 2300 m below sea level. In addition, we impose a radially symmetric 10°C temperature perturbation at the base of the model (z=-3350 m) centered at E, N = (0, 500) m tapering to zero at 3000 m laterally, with a $0.5 + 0.5 \cos(\pi r/3000)$ horizontal radial dependence, for r < 3000 m, and run 10^6 years to allow temperatures and pressures to stabilize. Resulting temperatures are plotted in Figure 10. At reservoir depth (-1005 m elev.), temperatures match observed temperatures at well locations within about 10°C, and at shallow depth (1107 m elev.) agreement at well locations is within about 20°C.
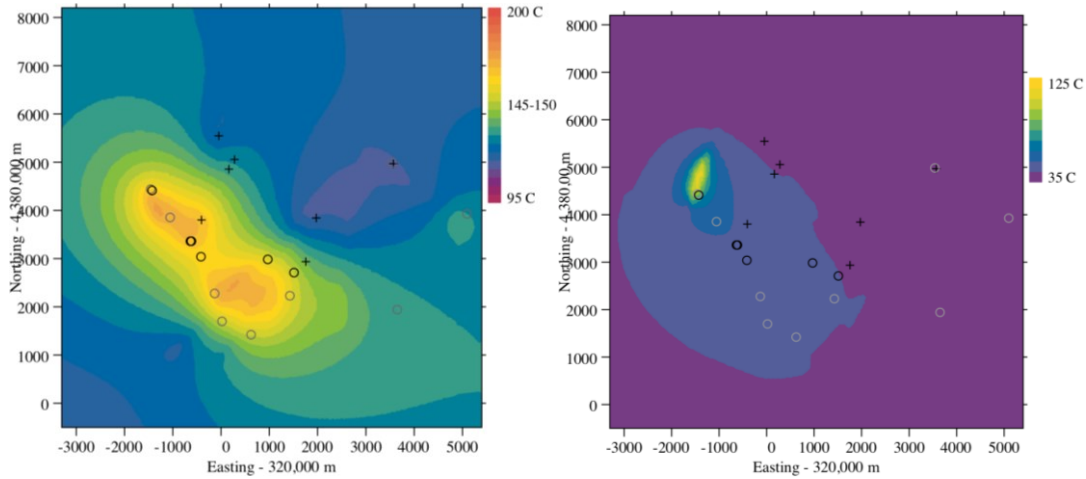

Figure 10: Left: simulated native-state temperatures at -1005 m elevation (reservoir depth). Right: simulated native-state temperatures at 1107 m elevation. Injection wellhead locations: crosses; production wellhead locations: black circles; other open wellhead locations: gray circles.

9. FLOW TEST DATA AND SIMULATION

Garg et al. (2015) show about 350 hours of data from two wells, 23-17 with wellhead at (-46, 5546) m, and 88-19 with wellhead at (-416, 3040), for roughly 200 hours of discharge of 110-120 kg/s from well 44-21, wellhead at (1973, 3844), and reinjection of 40-55 kg/s in well 37-17 ST1, wellhead at (161, 4856). We have simulated in this in the above model. At well 23-17, simulation results in a maximum observed increase in pressure of 237 kPa (34 psi) about 6 times larger than observed. At well 88-19, simulation results in a maximum magnitude change in pressure of +24 kPa (3.5 psi) of similar magnitude as observed (-16 kPa), but opposite sign. The

Smith et al.

simulated pressure at well 23-17 might be decreased by decreasing the background rock permeability locally between faults striking N -173.0 and N 23.8 (labeled in Fig. 1). To switch the sign of simulated pressure change at well 88-19, it would appear expedient to reduce the modelled permeability of the fault striking N 23.8 E or the southern portion thereof, as this extends most of the way from well 37-17 ST1 towards well 88-19, or that of the fault striking N -16.4, as that extends from the previous fault to well 88-19.

10. CONCLUSIONS

A 12-fault model derived from fitting well observations of large fractures, and zones of lost drilling circulation fits observed native-state well temperatures at reservoir depth (-1005 m elev.) to about 10°C, and at shallow depth (1107 m elev.) to about 20°C. However, it appears to need some local refinement to better match reported well test pressures.

ACKNOWLEDGMENTS

APPENDIX

Table 2: Fault plane (center) coordinates, before adjustment of edges, and number of fault intersection points supporting each plane. Strike is relative to Northing direction. Breadth is extent along dip.

Strike (deg.)	Dip (deg.)	x (m)	y (m)	z (m)	Length (m)	Breadth (m)	# points
18.2	67.1	-1350	4898	991	1973	608	5
-172.1	74.8	-377	4224	-746	3240	1496	10
150.0	81.6	-1349	4232	-576	1013	1772	8
23.8	72.1	21	4471	-1234	2869	805	5
-173.0	72.0	-36	4867	-718	2537	2705	4
-158.8	73.5	1422	2759	-1040	2787	1781	9
-137.1	71.1	318	2504	-1072	3830	2298	6
-16.4	72.5	-435	2876	-421	2540	2103	6
-27.4	87.4	-494	2950	-272	2687	2655	4
-146.1	55.0	817	2159	-959	2965	1819	4
-178.5	49.4	2628	3065	-911	3190	3370	4
127.1	81.0	4055	4541	-631	2701	1819	3

Table 3: Fault plane (center) coordinates, after adjustment of edges

Strike (deg.)	Dip (deg.)	x (m)	y (m)	z (m)	Length (m)	Breadth (m)
18.2	67.1	-1267	4871	786	1973	1053
-172.1	74.8	-574	4251	-1476	3239	3008
150.0	81.6	-1416	4193	-1108	1013	3677
23.8	72.1	214	4386	-1889	2869	2181
-173.0	72.0	-36	4867	-718	2537	2705
-158.8	73.5	1305	2804	-1464	3187	3052
-137.1	71.1	222	2593	-1456	4230	3110
-16.4	72.5	-435	2876	-421	2540	2103
-27.4	87.4	-494	2950	-272	2687	2255

-146.1	55.0	462	2398	-1570	2965	3312
-178.5	49.4	2628	3065	-911	3190	3370
127.1	81.0	3988	4453	-1330	2701	3234

REFERENCES

Cladouhos, T.T., Uddenberg, M.W., Swyer, M.W., Nordin, Y., and Garrison, G.H., 2017. Patua geothermal geologic conceptual model, GRC Transactions, Vol. 41.

Garg, S.K., Goranson, C., Johnson, S., and Casteel, J., 2015. Reservoir testing and modeling of the Patua geothermal field, Nevada, USA, Proceedings World Geothermal Congress 2015, Melbourne, Australia.

Glover, P., undated. Leeds Univ., Petrophysics MSc Course Note, undated course notes.

Isherwood, D. Harrar, J., and Raber, E., 1982. Characterization of Climax granite ground water, Lawrence Livermore National Laboratory, Livermore, Calif., UCRL-53309.

Izett, G.A., 1960. "Granite" Exploration Hole, Area 15, Nevada Test Site, Nye County, Nevada--Interim report, Part C, Physical properties, Trace Elements Memorandum Report 836-C, U.S. Depart. of Interior, Geological Survey.

Lutz, S.J., Hickman, S., Davatzes, N., Zemach, E., Drakos, P., and Robertson-Tait, A., 2010. Rock mechanical testing and petrologic analysis in support of well stimulation activities at the Desert Peak geothermal field, Nevada. Proceedings, 35th Workshop on Geothermal Reservoir Engineering, Stanford University, Stanford, CA.

Murphy, J., Holt, R., and Morrison, M., 2017. A numerical model case study of the Patua geothermal field, GRC Transactions, Vol. 41.

Pollack, A., 2020. Quantifying Geological Uncertainty and Optimizing Technoeconomic Decisions for Geothermal Reservoirs. PhD. Dissertation, Stanford University.

Pollack, A., Cladouhos, T.T., Swyer, M.W., Siler, D., Mukerji, T., and Horne, R.N., 2021. Stochastic inversion of gravity, magnetic, tracer, lithology, and fault data for geologically realistic structural models: Patua geothermal field case study, Geothermics, 95, 102129. (Fault marker data: https://github.com/ahinoamp/PyNoddyInversion/tree/master/code/Data/MarkersInversion.csv)

Raymer, L.L., Hunt, E.R. and Gardener, J.S., 1980. An improved sonic transit time-to-porosity transform, SPWLA Twenty-First Annual Logging Symposium.

Sewlvadurai, A.P.S., 2021. On the poroelastic Biot coefficient for a granitic rock, Geosciences, 11, 219.

Smith, J.T., Sonnenthal, E., and Majer, E., 2021. Modelling Pohang, South Korea, geothermal well stimulations and seismicity, GRC Transactions, Vol. 45.

Sonnenthal, E., Pettitt, W., Smith, T., Riahi, A., Siler, D., Kennedy, M., Majer, E., Dobson, P., Ayling, B., Damjanac, B., and Blankenship, D., 2018. Continuum thermal-hydrological-mechanical modeling of the Fallon FORGE site, GRC Transactions, Vol. 42.

Stowe, R.L., 1969. Strength and deformation properties of granite, basalt, limestone and tuff at various loading rates, Miscellaneous paper C-69-1, U.S. Army Engineer Waterways Experiment Station, Corps of Engineers, Vicksburg, Mississippi. https://usace.contentdm.oclc.org/digital/api/collection/p266001coll1/id/5682/download